IOSR Journal of Engineering (IOSRJEN) **www.iosrjen.org**
ISSN (e): 2250-3021, ISSN (p): 2278-8719
Vol. 06, Issue 06 (June. 2016), ||V1|| PP 48-61

Simulation of flow Through Layered Porous Media

R.A. Ford [a] , M.S. Abu Zaytoon [b] , M.H. Hamdan [c]

[a] *(School of Information Technology, College of the North Atlantic – Qatar, P.O. Box 24449, Doha,*

[b,c] *(Department of Mathematical Sciences, University of New Brunswick, P.O. Box 5050, Saint John, New Brunswick, Canada E2L 4L5*

***Abstract:* -** In this work, we consider the problem of fluid flow through layered porous media. A generalized algorithm is developed to handle flow through a finite number of layers and is based on casting the governing equation in a binary form that incorporates flow parameters capable of generating the Navier-Stokes equations as well as the well-known models of flow through porous media. A finite difference scheme of third-order accuracy is developed for the velocity and shear stress at the interfaces between layers, and numerical solution is obtained for a number of configurations involving flow in a two-dimensional channel bounded below and above by porous layers.

Keywords: - *Coupled parallel flow; Numerical algorithm.*

I. INTRODUCTION

Interest in coupled parallel flow through porous layers stems out of a large number of natural and industrial applications, including flow of groundwater in layered media, flow of oil in reservoirs and into production wells, blood flow through lungs and other human tissues, porous ball bearing, lubrication mechanisms with porous lining, in addition to heat and mass transfer processes across porous layers and their industrial applications (cf. [1-10] and the references therein). More recently, there has been an increasing interest in flow through and over porous layers of variable permeability in an attempt to provide more realistic descriptions of naturally occurring layered media (cf. [11-16]), using Darcy's equation and non-Darcian flow models [20-24]The problem of Darcy flow through two layers of different permeabilities has received considerable attention in groundwater literature (cf. [17-19]). In fact, this problem has been reported in the pioneering work of Polubarinova-Kochina [1]. The use of a non-Darcy model in the study of flow through layered media was first considered by Vafai and Thiagarajah [4] who provided theoretical and experimental analysis to better understand the phenomenon and to validate some of the available results when a non-Darcy model is used. Vafai and Thiagarajah [4], Allan and Hamdan [17], and Ford and Hamdan [19], considered the flow through two porous layers with flow being governed by the same model or by two different models.

Variations of the studies initiated in [4] include flow through two or more porous layers governed by same or different models. This problem is the subject matter of this work in which we consider fluid flow through a two-dimensional channel bounded below and above by porous layers, shown in **Fig. 1**. The analysis is valid for flow through any finite number, N, of porous layers, shown in **Fig. 2**. Flow through the channel (free space) is governed by the Navier-Stokes equations, and the flow through the porous layers is governed by a non-Darcy type model.

The available models of flow through porous media are cast in a generalized binary equation, and a general numerical algorithm is developed to handle flow through any finite number of layers. Matching conditions on the velocity and shear stress at the interface between two layers are implemented in a general form, [23], and finite difference expressions for the velocity and shear stress at the interface are developed. A numerical experiment is then carried out to simulate flow through channels and layered media involving three layers. In terms of the terminology of Parvazinia *et. al.* [10], our emphasis will be on the Brinkman and the free flow regions as is reflected by the choice of dimensionless permeability values (Darcy number) used in the current work.

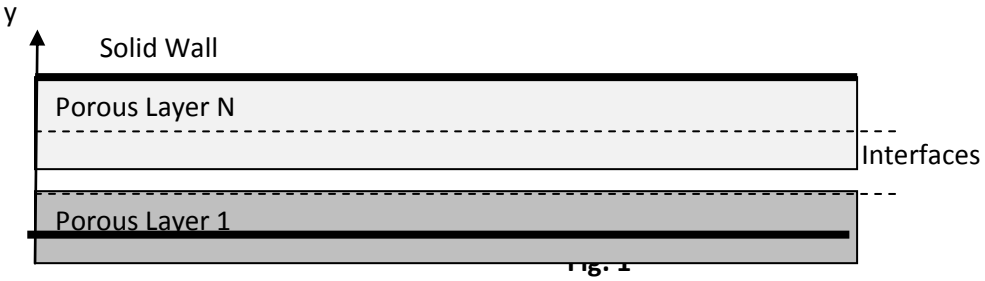

Fig. 1

Representative Sketch: Composite Porous Layers

II. PROBLEM FORMULATION

The steady motion of a viscous, incompressible fluid through isotropic porous material may be described by the following continuity and momentum equations, respectively

$$\nabla . \vec{v} = 0 \tag{1}$$

$$\rho[\beta(\eta - 1) + 1](\vec{v}.\nabla)\vec{v} = -\nabla p + \mu[\beta(\vartheta - 1) + 1]\nabla^2 \vec{v} - \beta\left\{\frac{\mu}{k}\vec{v} + \frac{\rho\sigma}{\sqrt{k}}\vec{v}\left|\vec{v}\right|\right\} \tag{2}$$

where $\vec{v}$ is the velocity vector, p is the pressure, k is the constant permeability, μ is the fluid viscosity, $\vartheta = \frac{\mu_e}{\mu}$, μ_e is the effective viscosity (that is, viscosity of the fluid in the porous medium), β is a binary parameter whose value is 0 if the flow is in free-space and 1 if flow is in the porous medium, σ is the form drag coefficient associated with the Forchheimer equation, η is a parameter whose values are discussed below, ∇ is the gradient operator, and ∇^2 is the Laplacian operator.

We remark here that the value of the parameter $\vartheta = \frac{\mu_e}{\mu}$ is dependent on the porous structure employed. While Brinkman [21] favoured the use of $\vartheta = 1$, some authors argue that μ and μ_e should be different, (cf. [24] and the references therein), to reflect the effect of introducing a solid matrix to the flowing fluid, which has the effect of enhancing the drag or offering the fluid less window. In either case, we formulate our current problem in general, and let the parameter ϑ enter the formulation. However, for the sake of numerical simulation, we assign a value of unity to ϑ.

For different choices of the parameters in (2), we recover the following forms of momentum equations that govern fluid flow in different regiments:

a) When $\beta = 0$ and $\vartheta = 1$, the Navier-Stokes (NS) equations are recovered.

b) When $\beta = 1$, $\eta = 0$, $\vartheta = 0$, and $\sigma = 0$, equations (2) reduce to Darcy's law (DE).

c) When $\beta = 1$, $\eta = 0$, $\vartheta = 0$, and $\sigma \neq 0$, equations (2) reduce to the Darcy-Forhheimer (DF) quation. (Note that the Darcy-Forchheimer equation accounts for the inertial effects in porous media through the introduction of a form drag coefficient and quadratic form inertial effects into Darcy's law).

d) When $\beta = 1$, $\eta = 1$, $\vartheta = 0$, and $\sigma = 0$, equations (2) reduce to Darcy-Lapwood (DL) equation.

e) When $\beta = 1$, $\eta = 1$, $\vartheta = \frac{\mu_e}{\mu}$, and $\sigma = 0$, equations (2) reduce to Darcy-Lapwood-Brinkman (DLB) equation. (Note that if we take $\eta = 0$ in this case then we recover the well-known Brinkman's equation DB).

f) When $\beta = 1$, $\eta = 1$, $\vartheta = \frac{\mu_e}{\mu}$, and $\sigma \neq 0$, equations (2) reduce to the Darcy-Lapwood-Forchheimer-Brinkman (DLFB) equation. (Note that if we take $\eta = 0$ in this case then we recover the Darcy-Forchheimer-Brinkman's (DFB) equation).

For convenience and ease of reference, we summarize the above cases, for the various parameters, in

Table 1. The "form drag coefficient", σ , that is associated with the Forchheimer equation, has been argued to asymptotically approach the value of 0.55, [2], [22]. In **Table 1**, we use this value of σ .

β	η	ϑ	σ	**Resulting Equation**
0	1	1	0	NS
1	0	0	0	DE
1	0	0	0.55	DF
1	1	0	0	DL
1	1	μ_e / μ	0	DLB
1	0	μ_e / μ	0	DB
1	1	μ_e / μ	0.55	DLFB
1	0	μ_e / μ	0.55	DFB

Table 1. Acronyms of Resulting Equations for Various Parameters

(NS: Navier-Stokes; DE: Darcy's equation; DF: Darcy-Forchheimer; DL: Darcy-Lapwood; DB: Darcy-Brinkman; DLB: Darcy-Lapwood-Brinkman; DFB: Darcy-Forchheimer-Brinkman; DLFB: Darcy-Lapwood-Forchheimer-Brinkman).

The classification summarized in **Table 1** shows that the Brinkman equation, the Darcy-Lapwood-Brinkman, the Darcy-Forchheimer-Brinkman, and the Darcy-Lapwood-Forchheimer-Brinkman models are the only equations of flow through porous media that account for viscous shear effects (hence, compatible with the presence of a macroscopic boundary on which a vanishing normal velocity can be imposed). Furthermore, the order of each of these equations is compatible with that of the Navier-Stokes equations. Hence, each of these equations is compatible with the imposition of velocity and shear stress continuity at the interface between a Navier-Stokes regime and a porous regime. They are also compatible with each other, thus allowing for velocity and shear stress continuity condition when different porous layers are superposed.

Now, considering the flow to be in two space dimensions, *x* and *y*, and taking $\vec{v} = (u, v)$, equation (1) takes the form:

$$u_x + v_y = 0 \tag{3}$$

and the momentum equations (2) can be expressed in components' form, as follows:

$$\rho[\beta(\eta - 1) + 1](uu_x + vu_y) = -p_x + \mu[\beta(\vartheta - 1) + 1](u_{xx} + u_{yy}) - \beta\left\{\frac{\mu}{k}u + \frac{\rho\sigma}{\sqrt{k}}u\sqrt{u^2 + v^2}\right\} \tag{4}$$

$$\rho[\beta(\eta - 1) + 1](uv_x + vv_y) = -p_y + \mu[\beta(\vartheta - 1) + 1](v_{xx} + v_{yy}) - \beta\left\{\frac{\mu}{k}v + \frac{\rho\sigma}{\sqrt{k}}v\sqrt{u^2 + v^2}\right\}. \tag{5}$$

For plane, parallel, fully-developed flow through a straight channel of depth *D*, bounded from above and below by solid impermeable walls, and extending in the *x*-direction, the following relations hold:

$$\begin{cases} v = v_x = v_{xx} = 0 \\ u = u(y) \\ u_x = u_{xx} = 0 \\ p = p(x) \\ p_y = 0 \end{cases} \tag{6}$$

Using (6), we find that the continuity equation (3) and the *y*-momentum equation (5) are automatically satisfied, and the *x*-momentum equation (4) reduces to:

$$-p_x + \mu[\beta(\vartheta - 1) + 1]u_{yy} - \beta\left\{\frac{\mu}{k}u + \frac{\rho\sigma}{\sqrt{k}}u|u|\right\} = 0. \quad (7)$$

Now, assume that the channel contains *N* layers, each of thickness L_i, for *i* = 1, 2, …, N, as depicted in **Fig. 2**, such that $\sum_{i=1}^{N} L_i = D$. The layers can be of different porous structures the flow through which is governed by a different flow model, or of the same porous structure with the flow through each layer being governed by the same flow model but with different permeability. It is also possible in this configuration for two porous layers to sandwich a free-space channel, the flow through which is governed by Navier-Stokes equations.

y = *N* _____(Solid Wall)
Layer N
y = *N-1* ----------
.
.
y = *i+1*----------
Layer *i+1*
y **= *i*** ---------- (Porous Interface)
Layer *i*
y = *i-1*----------
.
.
y = 1----------
Layer 1
y = 0 _____(Solid Wall)

Fig. 2. Representative Sketch: N Porous Layers

In order to customize equation (7) to each layer, it is first rendered dimensionless with respect to a characteristic length, L_i, for each layer, and a common characteristic velocity, u_c, using the following definitions:

$$(x^*, y^*) = \frac{(x, y)}{L_i}; u_i^* = \frac{u_i}{u_c}; k_i^* = \frac{k_i}{L_i^2}; p_i^* = \frac{p_i}{\rho_i (u_c)^2}; \mathrm{Re}_i = \frac{\rho_i u_c L_i}{\mu_i}. \quad (8)$$

While this "customization" emphasizes a definition of a Reynolds number that is appropriate for the flow in each layer, thus taking into account the possibility of different fluids of differing properties saturating each layer and moving at different speeds, we will consider in this work that the fluid saturating each layer is the same and flowing under the same applied pressure gradient.
Using (8) in (7) and dropping the "asterisks", we obtain the following dimensionless equation, valid for each layer, with the parameters assigned subscript *i* (for ease of reference) to the *ith* layer:

$$\frac{d^2 u_i}{dy^2} = \frac{\mathrm{Re}_i C_i}{\vartheta_i[1 + \beta_i(\vartheta_i - 1)]} + \frac{\beta_i u_i}{\vartheta_i k_i[1 + \beta_i(\vartheta_i - 1)]} + \frac{\beta_i \mathrm{Re}_i \sigma_i u_i^2}{\vartheta_i \sqrt{k_i}[1 + \beta_i(\vartheta_i - 1)]} \quad (9)$$

where $C_i < 0$ is the dimensionless pressure gradient associated with each layer (which, in this work, will be taken to be the same for all layers).
With the above normalization of variables and lengths, the depth of each layer becomes a dimensionless unity, as depicted in **Fig. 2**, and the depth of the layers can be described using the following intervals (under the assumption of a sharp interface between each pair of layers):

Layer 1 occupies the interval $0 \le y \le 1$

Layer 2 occupies the interval $1 \le y \le 2$

Layer *i* occupies the interval $i - 1 \le y \le i$

Layer N occupies the interval $N - 1 \le y \le N$.

The interface between each pair of consecutive layers occurs at *y* = 1, 2, 3, …, N-1. Furthermore, the lower and upper solid walls of the channel are located at *y* = 0 and *y* = N, respectively.
Boundary conditions associated with equation (9) are as follows:

i) No-slip condition along the lower and upper walls of the channel, that is

$$u_1\Big|_{y=0} = u_N\Big|_{y=N} = 0. \tag{10}$$

ii) Continuity of the velocity at the interface between layer *i* and layer *i+1*, namely

$$u_i\Big|_{y=i} = u_{i+1}\Big|_{y=i}, \text{ for } i = 1, 2, 3, \ldots, \text{N-1}. \tag{11}$$

iii) Continuity of the shear stress at the interface between layer *i* and layer *i+1*, namely

$$\vartheta_i \frac{du_i}{dy}\Big|_{y=i} = \vartheta_{i+1} \frac{du_{i+1}}{dy}\Big|_{y=i}, \text{ for } i = 1, 2, 3, \ldots, \text{N-1}. \tag{12}$$

III. NUMERICAL SOLUTION METHODOLOGY

The finite difference approach to (9) is rather straight forward. Each interval $i-1 \le y \le i$ is divided into subintervals of uniform step size *h*, and the grid points are numbered $j = 1,2,3,\ldots, m_i$, with grid point m_i coinciding with the interface between layer *i* and layer *i+1*. Equation (9) is then discretized using second-order accurate three point central differencing for the second derivative, and cast in the matrix-vector form

$$(A)_i u_j = -h^2 (B_i)_j \; ; \; j = 2, 3, \ldots, m_i - 1, \tag{13}$$

where $(A)_i$, is the tri-diagonal matrix given by

$$(A)_i = Trid \left[-1, 2 + \left(\frac{h^2 \beta_i}{\vartheta_i k_i [1 + \beta_i (\vartheta_i - 1)]} \right), -1 \right] \tag{14}$$

and

$$(B_i)_j = -\frac{h^2 \, \mathrm{Re}_i \, C_i}{\vartheta_i [1 + \beta_i (\vartheta_i - 1)]} - \frac{h^2 \beta_i \, \mathrm{Re}_i \, \sigma_i}{\vartheta_i \sqrt{k_i} [1 + \beta_i (\vartheta_i - 1)]} (u_i^2)_j . \tag{15}$$

At each interface, $j = m_i$, the velocity at the interface, $(u_m)_i$ is a quantity to be determined.

The solution algorithm proceeds as follows.

Step 1: Initialize $(u_m)_i$, for *i* = 1, 2, …, N-1, and assign values to the parameters appropriate for each layer.

Step 2: Initialize u_i at all internal grid points $j = 2, 3, \ldots, m_i - 1$, for *i* = 1, 2, …, N-1.

Step 3: For *i* = 1, 2, …, N-1:

3.1) Solve (13) iteratively for $(u_i)_j$, $j = 2, 3, \ldots, m_i - 1$, using the Tri-diagonal Solver and Successive Over-relaxation.

3.2. Update $(u_m)_i$.

Step 4: Repeat Step 3 until $\sum_{j=2}^{m_i - 1} \left| (u_i)_j^{\,n} - (u_i)_j^{\,n-1} \right| < \varepsilon$, for *i* = 1, 2, …, N-1, where *n* is the iteration level and $\varepsilon = 5 \times 10^{-5}$ is the error tolerance.

In order to update $(u_m)_i$, in Step 3, we implement the conditions at the interface, namely (11) and (12), in developing finite difference approximations for $(u_m)_i$ in terms of the values of u_i, at grid points in the vicinity of the *ith* interface. These are given in the following sub-section.

Finite difference expressions for the velocity, $(u_m)_i$, at the interface between layer *i* and layer *i+1* are obtained using third-order accurate scheme for the shear stress matching condition (12). This choice of order is based on the recommendations given in [26], where they deemed a third-order accurate scheme preferable when dealing with the shear stress computation.

Forward and backward difference schemes for the first derivative of the velocity with respect to *y* are set equal at each interface and expressions for $(u_m)_i$ are obtained in terms of the in-field quantities of the two neighbouring layers. Finite difference expressions are then obtained using the derivatives of equation (9) and the Taylor's series expansions about grid-point m_i *(*for each interface between layer *i* and layer *i+1*), as follows.

From (9), we have

$$\frac{d^3u_i}{dy^3} = \frac{\beta_i}{\vartheta_i k_i[1+\beta_i(\vartheta_i-1)]}\frac{du_i}{dy} + \frac{2\beta_i \,\mathrm{Re}_i\,\sigma_i}{\vartheta_i\sqrt{k_i}[1+\beta_i(\vartheta_i-1)]}u_i\frac{du_i}{dy} \tag{16}$$

$$\frac{d^4u_i}{dy^4} = \frac{\beta_i}{\vartheta_i k_i[1+\beta_i(\vartheta_i-1)]}\frac{d^2u_i}{dy^2} + \frac{2\beta_i \,\mathrm{Re}_i\,\sigma_i}{\vartheta_i\sqrt{k_i}[1+\beta_i(\vartheta_i-1)]}\left[u_i\frac{d^2u_i}{dy^2} + \left(\frac{du_i}{dy}\right)^2\right] \tag{17}$$

Now, from Taylor's series, we have the following expansions

$$u_{m\mp1}\big|_i = u_m \mp h(u_y)_m + \frac{h^2}{2}(u_{yy})_m \mp \frac{h^3}{6}(u_{yyy})_m + \frac{h^4}{24}(u_{yyyy})_m \mp \ldots \tag{18}$$

$$u_{m\mp2}\big|_i = u_m \mp 2h(u_y)_m + 2h^2(u_{yy})_m \mp \frac{4h^3}{3}(u_{yyy})_m + \frac{2h^4}{3}(u_{yyyy})_m \mp \ldots \tag{19}$$

$$u_{m\mp3}\big|_i = u_m \mp 3h(u_y)_m + \frac{9h^2}{2}(u_{yy})_m \mp \frac{9h^3}{2}(u_{yyy})_m + \frac{27h^4}{8}(u_{yyyy})_m \mp \ldots \tag{20}$$

Using (18), (19), (20), we obtain the following third-order accurate expressions for $(u_y)_m$ valid in layer *i*:

$$(u_y)_m\big|_i = \frac{-2(u_{m-3})_i + 9(u_{m-2})_i - 18(u_{m-1})_i + 11(u_m)_i}{6h} - \frac{3h^3}{2}(u_{yyyy})_m\big|_i + H.O.T. \tag{21}$$

and the following expressions valid in layer *i+1:*

$$(u_y)_m\big|_{i+1} = \frac{2(u_{m+3})_{i+1} - 9(u_{m+2})_{i+1} + 18(u_{m+1})_{i+1} - 11(u_m)_{i+1}}{6h} - \frac{3h^3}{2}(u_{yyyy})_m\big|_{i+1} + H.O.T \tag{22}$$

where *H.O.T.* stands for *Higher Order Terms*.

Using conditions (11) and (12) in expressions (21) and (22), and solving for $(u_m)_i$, we obtain the following third-order accurate scheme together with the associated leading error term, *E*:

$$(u_m)_i \cong \frac{\vartheta_i}{11(\vartheta_i+\vartheta_{i+1})}[2(u_{m-3})_i - 9(u_{m-2})_i + 18(u_{m-1})_i]$$

.

$$+ \frac{\vartheta_{i+1}}{11(\vartheta_i+\vartheta_{i+1})}[2(u_{m+3})_{i+1} - 9(u_{m+2})_{i+1} + 18(u_{m+1})_{i+1}]$$

$$E = \frac{\vartheta_i}{11(\vartheta_i+\vartheta_{i+1})}9h^4(u_{yyyy})_m\big|_i - \frac{\vartheta_{i+1}}{11(\vartheta_i+\vartheta_{i+1})}9h^4(u_{yyyy})_m\big|_{i+1}$$

The leading error terms, (24), is evaluated using the expressions for the derivatives given by equations (9), (16) and (17).

It is clear that the derivations given above emphasize a significant relationship between the flow parameters and the finite difference schemes. The leading error term in the local truncation error is a function of the flow parameters, the step size, and the velocity and shear stress at the interface.

IV. RESULTS AND DISCUSSION

Results have been obtained for three main flow configurations involving flow in a channel (as governed by Navier-Stokes equations) bounded from above and from below by porous layers, as shown in **Fig.**

1. The first configuration is when the flow through both porous layers is governed by the Darcy-Lapwood-Brinkman model. The second is when the flow through both porous layers is governed by the Darcy-Forchheimer-Brinkman model, and the third configuration is when the flow in one layer is governed by the Darcy-Lapwood-Brinkman model, and flow in the other layer is governed by the Darcy-Forchheimer-Brinkman model. For the sake of comparison, we also consider the Navier-Stokes flow through a channel past a single porous layer when the flow through the porous layer is governed by the DLB model in one case and by the DFB model in another case. This will afford us a comparison between flow in channels bounded by one or two layers.

To accomplish the above, we take a combination of the dimensionless permeability values $k = 0.0001$, $k = 0.01$, and $k = 1$. We will refer to the dimensionless permeability of the lower layer by k_l, and that of the upper layer by k_u. For flow over a single porous layer, we also test the dimensionless permeability values $k = 10$ and $k = 100$. Furthermore, and without loss of generality of the approach, we assign the following values to the flow and media parameters (for all cases tested): Re = 10; C = -2 or -10; $\sigma = 0.55$, and $\vartheta = 1$.

Flow over a single porous layer:

Velocity and shear stress results obtained for the two combinations: DLB/NS and DFB/NS are illustrated in **Table 2(a)** and **2(b)**, respectively, and demonstrate the following observation for both cases: increasing the permeability results in increasing the velocity at the interface, and in decreasing the shear stress at the interface. For lower permeability, the flow through the porous layer is slower, and the boundary layer near the interface is thinner, thus resulting in a higher shear stress effects at the interface. Continuity of velocity at the interface causes the Navier-Stokes flow in the channel to slow down near the interface and to adjust to the slower flow in the low-permeability porous layer. As permeability increases, the speed of the flow in the porous layer increases, and continuity of velocity at the interface results in a higher velocity value in the channel in interfacial region. Furthermore, for higher permeability, the boundary layer near the interface is thicker, thus resulting in a lower shear stress there.

k	u_m	$(u_y)_m$
0.0001	0.566855	49.432662
0.01	5.456965	44.542608
1	41.595070	8.404662

Table 2(a). Velocity and Shear Stress at the interface: DLB/NS for different permeability values.

$h = 0.01; \vartheta = 1; \text{Re} = 10; C = -10$.

k	u_m	$(u_y)_m$
0.0001	0.564110	49.435380
0.01	3.503863	46.495678
1	9.214851	40.784737

Table 2(b). Velocity and Shear Stress at the interface: DFB/NS for different permeability values.

$h = 0.01; \sigma = 0.55; \text{Re} = 10; C = -10$.

The fully-developed flow pattern through a channel past a single porous layer is illustrated in **Fig. 3**, when the flow through the porous layer is governed by the DLB model, and in **Fig. 4** when the flow through the porous layer is governed by the DFB model. Both Figures show the effect of increasing permeability. For high permeability values, **Fig. 3** shows that the pattern is nearly symmetric about the interface. This may be attributed to the fact that the DLB model offers a good approximation to the Navier-Stokes equations when permeability is high. In fact, when the *dimensional* permeability approaches infinity, the DLB equation reduces to the Navier-Stokes equation, as can be seen from equation (2) or equation (7). For low permeability, the velocity through the porous layer tends to be uniform, as the DLB equation resembles Darcy's equation (which gives a uniform velocity profile through the porous layer).

Fig. 4 illustrates the velocity through the layer and in the channel for low and high dimensionless permeability in the DFB model. For low permeability, the parabolic flow velocity through the channel (as governed by Navier-Stokes) is slightly affected by the presence of the porous layer. Distortion to the parabolic pattern becomes more noticeable with increasing permeability, due to the corresponding increase in the velocity at the interface. The velocity in the porous layer, on the other hand, starts out as being close to uniform for low permeability. With increasing permeability, velocity distortion is more noticeable when using the DFB model (unlike the parabolic-like pattern that occurs when the DLB model is used). This distortion may be attributed to the microscopic quadratic inertial effects that arise in the Forchheimer model.

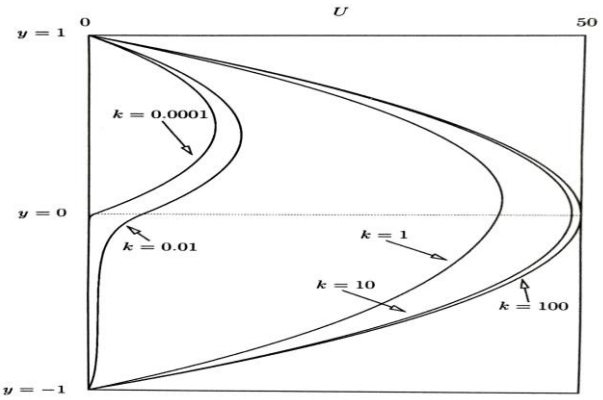

Fig. 3. Velocity profile for flow through NS-DLB layers; Re = 10, C= -10.

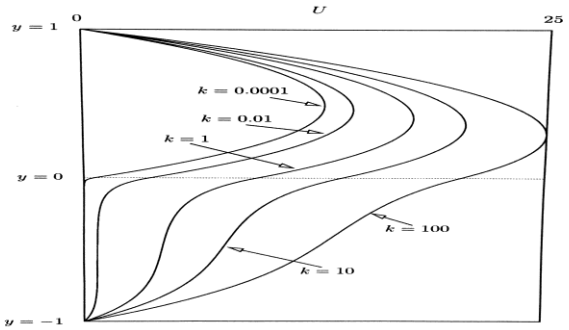

Fig. 4. Velocity profile for flow through DFB-NS layers; Re = 10, C= -10.

Values of velocity and shear stress at the interfaces between the porous layers and the free-space channel are illustrated in **Table 3** for the three configurations considered:
Configuration 1: Flow in both porous layers is governed by the DLB model.
Configuration 2: Flow in both porous layers is governed by the DFB model.
Configuration 3: Flow in one layer is governed by the DLB model and in the other by the DFB model.

Model equations	k_l	k_u	$(u)_{m1}$	$(u)_{m2}$	$(u_y)_{m1}$	$(u_y)_{m2}$
	0.0001	0.0001	0.114649	0.114649	9.999966	-9.999966
	0.01	0.0001	1.102823	0.125658	9.022743	-10.97716
	0.01	0.01	1.200611	1.200611	9.999952	-9.999952
DLB/NS/	0.01	1	1.923775	9.150725	17.22694	-2.772992
DLB	1	1	14.65478	14.65478	9.999969	-9.999969
DFB/NS/	0.0001	0.0001	0.114533	0.114533	9.999889	-9.999889
DFB	0.01	0.0001	0.938677	0.123697	9.184770	-10.81497
	0.01	0.01	0.999742	0.999742	9.999872	-9.999872
	0.01	1	1.157519	3.311800	12.15426	-7.845523
	1	1	3.684628	3.684628	9.999890	-9.999890
DLB/NS/	0.0001	0.0001	0.114648	0.114535	9.999853	-10.00008
DFB	0.01	0.01	1.183492	1.012469	9.828903	-10.17100
	1	1	10.30998	4.605344	4.295219	-15.70461

Table 3. Velocity and shear stress at the interfaces of the configuration in Fig. 2; different combinations of flow through multiple layers.

k_l : Permeability of lower porous layer; k_u : Permeability of upper porous layer.

$(u)_{m1}$: Velocity at lower interface; $(u)_{m2}$: Velocity at upper interface.

$(u_y)_{m1}$: Shear stress at lower interface; $(u_y)_{m2}$: Shear stress at upper interface.

Table 3 demonstrates the expected increase in the velocity at the interface with increasing permeability in each layer, for each of the above three configurations. However, for configurations 1 and 2, and unlike the case of

flow over a single layer, the associated decrease in the value of the shear stress is not apparent. This may be attributed to the presence of two bounding porous layers. The upper layer, say, affects the flow in the free-space channel, which in turn affects the flow in the lower layer. The shear stresses at the interfaces vary in response to the different combinations of permeability without a consistent pattern.

For configuration 3, one porous layer is governed by the DLB model and the other by the DFB. For the same permeability in each layer, **Table 3** shows increasing the permeability results in an increase in the velocity at the interface. The shear stress at the interface with the DLB layer decreases with increasing permeability. At the interface with the DFB layer, the shear stress increases, in absolute value, with increasing permeability. This may be attributed to the higher inertial effects associated with the DFB model and requires a higher shear for higher permeability. It is worth noting (as shown in **Table 2(a) and 2(b)**) that higher shear stress at the interface is associated with the DFB model than with the DLB model, for the same high permeability value.

Fig. 5 and **Fig. 6** illustrate the velocity profiles for configuration 1. Flow through the bounding porous layers is governed by the DLB model, and flow through the (middle) channel is governed by the Navier-Stokes equations. In **Fig. 5**, the permeability of the lower porous layer (k_l) is the same as the permeability of the upper porous layer (k_u).

Fig. 5 demonstrates symmetric velocity profiles for the range of permeability considered, and the expected increase in the velocity at the interfaces with increasing permeability. When the dimensionless permeability is unity, the velocity profile is parabolic in shape and resembles flow through a channel governed by Navier-Stokes equations and bounded by solid walls. Again, this enforces the concept that the DLB model approximates the Navier-Stokes equations for large permeability.

Fig. 6 illustrates the velocity profiles when permeability in the lower layer is fixed ($k_l = k_2 = 0.01$) and permeability of the upper layer takes the values $k_u = k_1 = 0.0001$; 0.01, and 1. **Fig. 6** demonstrates the loss of symmetry in the velocity profiles when the porous layers' permeability values are different. Furthermore, the layer with the higher permeability results in a larger velocity at the interface between that layer and the fluid layer in the channel. This results in a deviation from symmetry of the profiles.

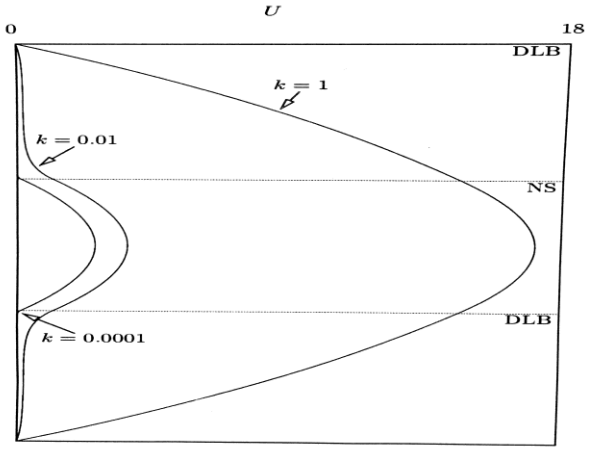

Fig. 5. Velocity profile for flow through DLB-NS-DLB layers with equal permeabilities; Re = 10, C= -2.

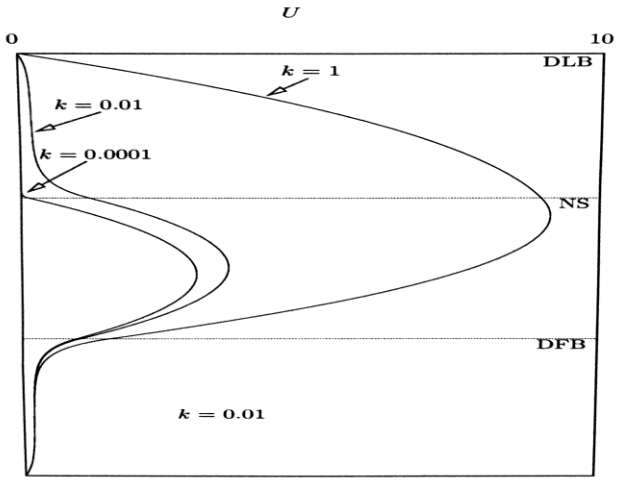

Fig. 6. Velocity profile for flow through DFB-NS-DLB layers with equal permeabilities; Re = 10, C= -2.

Fig. 7 and **Fig. 8** illustrate the velocity profiles for configuration 2. Flow through the bounding porous layers is governed by the DFB model, and flow through the channel is governed by the Navier-Stokes equations.

In **Fig. 7**, the permeability of the upper porous layer is the same as the permeability of the lower porous layer ($k_l = k_u = k$). **Fig. 7** demonstrates symmetric velocity profiles for the range of permeability considered, and the expected increase in the velocity at the interfaces with increasing permeability. Unlike the case of the DLB model illustrated in **Fig. 5**, the velocity profile is non-parabolic in the configuration for large permeability. Furthermore, the maximum velocity in the fluid layer (middle of the channel) when the DFB model is used is less than the corresponding maximum when the DLB model is used. In addition, the velocity at each interface for the DFB model is lower than the corresponding value for the DLB model, for the same permeability. This may be attributed to the higher inertial effects associated with the DFB model, which tend to slow down the flow in the porous layer, with the ultimate effect of reducing the velocity at the interface, and reducing the maximum velocity at mid-configuration. When the dimensionless permeability is unity, the velocity profiles in the porous layers are distorted in the DFB model, with the middle of each layer representing a point of inflection. While this distortion is not noticeable for low permeability values, where the profile is almost uniform and exhibits a behavior expected of the Darcy equation, it may point out to the fact the DFB model is more suitable for describing flow in low permeability media.

Fig. 8 illustrates the velocity profiles when permeability in the lower layer is fixed ($k_l = k_1 = 0.01$) and permeability of the upper layer takes the values $k_u = k_2 = 0.0001$; 0.01, and 1. **Fig. 8** demonstrates the loss of symmetry in the velocity profiles when the porous layers' permeability values are different. Furthermore, the layer with the higher permeability results in a larger velocity at the interface between that layer and the fluid layer in the channel. This results in a deviation from symmetry of the profiles, with the maximum velocity in the fluid layer no longer occurring in the middle of the channel.

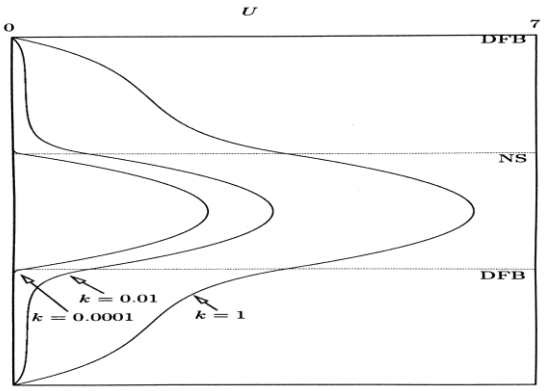

Fig. 7. Velocity profile for flow through DFB-NS-DFB layers with equal permeabilities; Re = 10, C= -2.

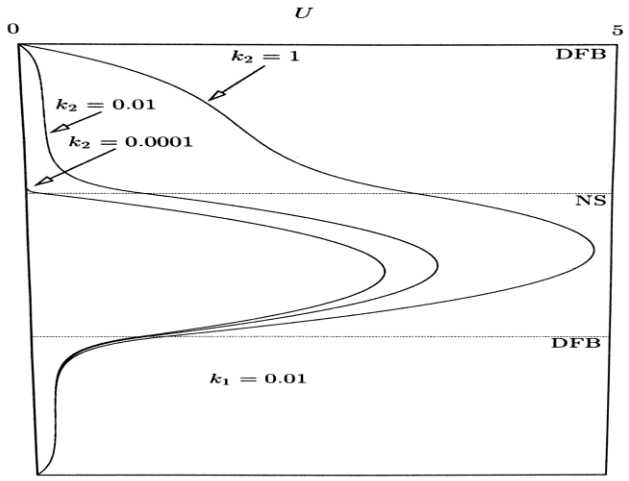

Fig. 8. Velocity profile for flow through DFB-NS-DFB layers; Re = 10, C= -2.

Fig. 9 and **Fig. 10** illustrate the velocity profiles for configuration 3, where flow through the lower bounding porous layer is governed by the DFB model, and flow through the upper bounding porous layer is governed by the DLB model. Again, flow in the fluid layer (middle section of the channel) is governed by the Navier-Stokes equations.

In **Fig. 9**, the permeability of the upper porous layer is the same as the permeability of the lower porous layer ($k_l = k_u = k$). **Fig. 9** demonstrates a velocity profile that is visually symmetric for low values of permeability.

This emphasizes that the Forchheimer inertial effects are less significant for low permeability, slow flow through porous media. Furthermore, for the low permeability values considered, both the DLB and DFB velocity profiles in the porous layers are close to being uniform, thus resembling the expected behaviour of the Darcy equation. However, as we get closer to the interface and closer to the macroscopic boundary where the no-slip condition is used, uniformity of the velocity profiles is lost. For larger values of permeability (*k = 1*), the velocity profile is distorted due to the higher inertial effects of the DFB model and the fact that flow through the layer governed by the DLB model is faster than the flow in the layer governed by the DFB model, for the same driving pressure gradient. This results in a higher velocity at the interface between the upper porous layer and the fluid layer in the channel. Furthermore, location of the maximum attained velocity shifts in the direction of the porous layer with higher flow velocity. This behaviour is further exhibited in **Fig. 10**, which illustrates the velocity profiles for a fixed permeability in the DFB layer, and different values of permeability in the DLB layer. The increase of the velocity at the interfaces with increasing permeability is evident, together with greater deviation from symmetry in response to increasing permeability in the DLB layer. Furthermore, location of the maximum velocity in the channel shifts towards the layer with the higher permeability.

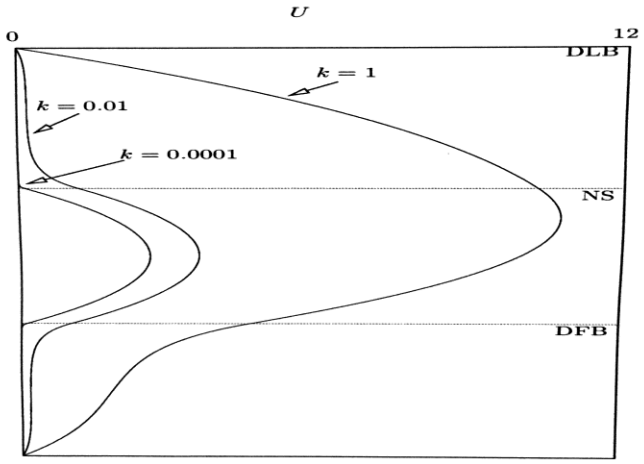

Fig. 9. Velocity profile for flow through DFB-NS-DLB layers with equal permeabilities; Re = 10, C= -2.

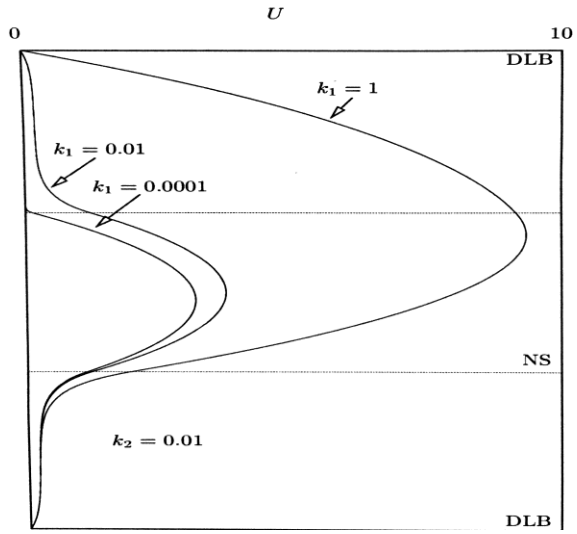

Fig. 10. Velocity profile for flow through DLB-NS-DLB layers; Re = 10, C= -2.

Effect of grid refinement

In Step 4 of the Solution Algorithm of **Section 3.1**, we employed an error tolerance of $\varepsilon = 5 \times 10^{-5}$ on the sum of absolute errors of all computed u values in a given layer. This guarantees computations that are four significant digits of accuracy. The finite difference procedure used for the governing differential equation is of order $O(h^2)$, and for the shear stress of order $hO(h^2)$. A choice of *h=0.01* is deemed sufficient to result in computations accurate to within four significant digits.

In order to validate the above, we conducted a numerical experiment to test the effect of grid refinement on the computed solution using the test case of flow through a channel (as governed by the Navier-Stokes equations) bounded by a finite porous layer the flow through which is governed by the Darcy-Lapwood-Brinkman model. For this DLB/NS combination, we used grid spacing *h=0.01, h=0.005,* and *h=0.002*. Computations obtained using these step sizes for the velocity and shear stress are compared with the exact solution obtained in [19], and reported in **Table 4**, which also contains evaluations of the leading error term for each step size.

Table 4 demonstrates an agreement in five significant digits of accuracy, for all step sizes used, between the computed and exact values of the velocity at the interface. For the shear stress at the interface, the agreement is in four significant digits, for *h=0.01*, and in five significant digits for the finer grid (*h=0.005* and *h=0.002*). Furthermore, the order of the leading error term is $O(10^{-6})$ for *h=0.01*. Within the error tolerance employed in this work, namely $\varepsilon = 5 \times 10^{-5}$, the desired accuracy in computations is obtained using *h=0.01*. This step size has therefore been used to obtain all reported results in this work.

Step-size h	u_m	$(u_y)_m$	**Leading error term**
0.01	41.595070	8.404662	-0.2389E-6
0.005	41.595225	8.404585	-0.2987E-7
0.002	41.595248	8.404561	-0.1911E-8
Exact Solution	41.595438	8.404562	

Table 4. Effect of Grid Refinement. DLB-NS combination

$k = 1; \vartheta = 1; \text{Re} = 10; C = -10$.

V. CONCLUSION

In this work, we presented a numerical methodology capable of simulating flow through a finite number of porous layers. A single binary equation was developed to describe the flow in the various layers and in free-space. With proper choices of the parameters, the governing equation can be solved numerically for any finite number of layers and channels. A third-order accurate finite differences scheme was developed for the shear stress and velocity at the interface between any two layers. The method was used in this work to simulate the flow through a channel bounded by two porous layers (of the same structure with differing permeability, and of differing structures with the same permeability). Comparison with the cases of flow over a single porous layer was made in this work to demonstrate the effect of introducing a second bounding layer on the shear stress

and velocity at the interface. The developed methodology, and the finite difference scheme, may prove to be of value when one considers two-dimensional flow simulation through layers, or flow through composite layers possessing curvilinear interfaces.

Velocity profiles for the flow in the different configurations considered support the following conclusions:

1) Location of the maximum velocity attained in the channel shifts towards the porous layer with higher permeability.
2) Velocity profile distortion and deviation from symmetry occurs when employing the DFB model in all chosen configurations. Deviation from symmetry for the DLB model occurs when the bounding porous layers possess different permeability values.
3) Velocities at the interfaces between the channel and the porous layers increase with increasing permeability, for a given pressure gradient and Reynolds number.
4) Both the DLB and DFB models exhibit compatible velocity profiles for low permeability. For high permeability, the DLB model approximates the Navier-Stokes equations, while inertial effects of the DFB model become more noticeable and cause greater distortion in the velocity profiles.
5) For flow through a channel bounded by a single porous layer, shear stress at the interface with the DLB porous layer decreases with increasing permeability. At the interface with the DFB porous layer, the shear stress increases, in absolute value, with increasing permeability due to the Forchheimer inertial effects associated with this model.

REFERENCES

[1] P.Y. Polubarinova-Kochina, Theory of Groundwater Movement, Princeton University Press, Princeton, NJ, 1962.

[2] N. Rudraiah, Coupled parallel flows in a channel and a bounding porous medium of finite thickness, *J. Fluids Eng. ASME, 107*, 1985, 322-329.

[3] K. Vafai and S.J. Kim, Fluid mechanics of the interface region between a porous medium and a fluid layer: an exact solution, *Int. J. Heat Fluid Flow*, *11(3)*, 1990, 254-256.

[4] K. Vafai and R. Thiyagaraja, Analysis of flow and heat transfer at the interface region of a porous medium, *Int. J. Heat Mass Transfer*, *30(7)*, 1987, 1391-1405.

[5] K. Vafai and C. L. Tien, Boundary and inertia effects on flow and heat transfer in porous media, *Int. J. Heat Mass Transfer*, *24*, 1981, 195-203.

[6] K. Vafai and C. L. Tien, Boundary and inertia effects on convective mass transfer in porous media, *Int. J. Heat Mass Transfer*, *25*, 1982, 1183-l190.

[7] D.D. Joseph, D.A. Nield and G. Papanicolaou, Nonlinear equation governing flow in a saturated porous medium, *Water Resources Res.*, *18*, 1982, 1049-1052.

[8] G. Neale, G. and W. Nader, Practical significance of Brinkman's extension of Darcy's law: coupled parallel flows within a channel and a bounding porous medium, *Canadian J. Chem. Eng.*, *52*, 1974, 475-478.

[9] D.A. Nield, The Limitations of the Brinkman-Forchheimer equation in modeling flow in a saturated porous medium and at an interface, *Int. J. Heat Fluid Flow*, *12(3)*, 1991, 269-272.

[10] M. Parvazinia, V. Nassehi, R. J. Wakeman, and M. H. R. Ghoreishy, Finite element modelling of flow through a porous medium between two parallel plates using the Brinkman equation, *Transport in Porous Media*, *63*, 2006, 71–90.

[11] M.S. Abu Zaytoon, T.L. Alderson and M.H. Hamdan**,** Flow through a layered porous configuration with generalized variable permeability, *Int. J. of Enhanced Research in Science, Technology & Engineering, 5(6)*, 2016, 1-21.

[12] M.S. Abu Zaytoon, T.L. Alderson and M. H. Hamdan, Flow through a Variable Permeability Brinkman Porous Core, *Journal of Applied Mathematics and Physics, 4*, 2016, 766-778.

[13] M.S. Abu Zaytoon, T.L. Alderson and M. H. Hamdan, Flow over a Darcy porous layer of variable permeability, *Journal of Applied Mathematics and Physics, 4*, 2016, 86-99.

[14] M.S. Abu Zaytoon, T.L. Alderson and M. H. Hamdan, Flow through layered media with embedded transition porous layer, , *Int. J. of Enhanced Research in Science, Technology & Engineering, 5(4)*, 2016, 9-26.

[15] M.S. Abu Zaytoon, T.L. Alderson and M. H. Hamdan, Flow through variable permeability composite porous layers, *Gen. Math. Notes, 33(1)*, 2016, 26-39.

[16] S.OAlharbi, T.L. Alderson and M.H. Hamdan, Coupled parallel flow of fluids with viscosity stratification through composite porous layers, *IOSR Journal of Engineering*, *6(5)*, 2016, 32-41.

[17] F.M. Allan, M.H. Hamdan, Fluid mechanics of the interface region between two porous layers, *Appl. Math. Comput.*, *128(1)*, 2002, 37-43.

[18] F.M. Allan and M.H. Hamdan, Arbitrary finite difference schemes for coupled parallel flow over porous layers, in: S.H. Sohrat, H.J. Catrakis and F.-K. Benra, (Eds.), *Theoretical and Experimental Aspects of Fluid Mechanics*, ISBN 978-960-6766-30-5, WSEAS Press, 2008, 246-253.

[19] R.A. Ford and M.H. Hamdan, Coupled parallel flow through composite porous layers, *Appl. Math. Comput. 97*, 1998, 261-271.

[20] G.S. Beavers and D.D. Joseph, Boundary conditions at a naturally permeable wall, *J. Fluid Mech. 30(1)*, 1967, 197-207.

[21] H.C. Brinkman, A Calculation of the viscous force exerted by a flowing fluid on a dense swarm of particles, *Appl. Scientific Res. A1*, 1947, 27-34.

[22] B.C. Chandrasekhara, K. Rajani and N. Rudraiah, Effect of slip on porous-walled squeeze films in the presence of a magnetic field, *Appl. Scientific Res. 34*, 1978 393-411.

[23] W.S. Almalki and M.H. Hamdan, Theoretical relationships of fluid and flow quantities in composite porous layers, *Int. Journal of Engineering Research and Applications*, 6(2), 2016, 10-21.

[24] W.S. Almalki and M.H. Hamdan, Investigations in effective viscosity of fluid in a porous medium, *Int. Journal of Engineering Research and Applications*, 6(4), 2016, 41-51.